

Large tunable valley splitting in edge-free graphene quantum dots on boron nitride

Nils M. Freitag¹, Tobias Reisch², Larisa A. Chizhova²,
 Péter Nemes-Incze^{1,3}, Christian Holl¹, Colin R. Woods⁴,
 Roman V. Gorbachev⁴, Yang Cao⁴, Andre K. Geim⁴,
 Kostya S. Novoselov⁴, Joachim Burgdörfer², Florian Libisch², and
 Markus Morgenstern¹

¹II. Institute of Physics B and JARA-FIT, RWTH Aachen University, Otto-Blumenthal-Straße, 52074 Aachen, Germany
²Institute for Theoretical Physics, TU Wien, Wiedner Hauptstraße 8-10, 1040 Vienna, Austria
³Centre for Energy Research, Institute of Technical Physics and Materials Science, Lendület - Topology in Nanomaterials Research Group, 1121 Budapest, Konkoly-Thege way 29-33, Hungary
⁴School of Physics & Astronomy, University of Manchester, Manchester M13 9PL, United Kingdom

Coherent manipulation of binary degrees of freedom is at the heart of modern quantum technologies. Graphene offers two binary degrees: the electron spin and the valley. Efficient spin control has been demonstrated in many solid state systems, while exploitation of the valley has only recently been started, yet without control on the single electron level. Here, we show that van-der Waals stacking of graphene onto hexagonal boron nitride offers a natural platform for valley control. We use a graphene quantum dot induced by the tip of a scanning tunneling microscope and demonstrate valley splitting that is tunable from -5 to +10 meV (including valley inversion) by sub-10-nm displacements of the quantum dot position. This boosts the range of controlled valley splitting by about one order of magnitude. The tunable inversion of spin and valley states should enable coherent superposition of these degrees of freedom as a first step towards graphene-based qubits.

Electrical control is a central requirement to exploit the binary degrees of freedom of a single electron in a scalable way¹. This has been realized for

spin systems using, e.g., small shifts of the electron spin within the field of a micro-magnet^{2,3}. The valley degree of electrons has recently been detected in transport experiments on graphene⁴⁻⁹, but its control on the single electron level has not been achieved. Alternative materials, such as Si¹⁰, offer only very small tuning ranges of the valley splitting by less than 0.5 meV^{5,11-15}.

The valley degree of freedom in graphene is a consequence of the honeycomb structure with its two atoms within the unit cell^{16,17}. Hence, breaking the equivalence of the two atoms (sublattice symmetry breaking) is the natural avenue to break the valley degeneracy as a starting point for tuning. This indeed works straightforwardly, if the time reversal symmetry is additionally broken, e.g., by a magnetic field B ¹⁸. The sublattice symmetry breaking can be achieved by van-der Waals stacking of 2D materials exploiting the different stacking of the two graphene atoms on top of the supporting atoms. This stacking moreover spatially varies due to the different lattice constants of the adjacent materials¹⁹⁻²¹, implying a spatially varying valley splitting which we exploit in our experiment.

We have recently demonstrated smoothly confined Dirac fermions in an edge-free graphene quantum dot (QD) by combining the electric field of the tip with a perpendicular B field (Fig. 1a)²². The B field quantizes the continuous spectrum of graphene in terms of Landau levels (LLs, LL spacing ≈ 100 meV at $B = 7$ T)¹⁸. The electric field of the tip exploits the energy gaps between LLs to achieve edge-free confinement, i.e., it shifts energy levels from the LLs into the gap²². We thereby overcome the well-known problem of edge localization within etched graphene QDs²³. By confining without resorting to physical edges, these dots preserve the two-fold valley and spin symmetries of pristine graphene (Fig. 1b, d).

The charging of the confined levels has been directly measured by tuning the voltage of the STM tip such that the states cross the Fermi level E_F . This revealed the most regularly spaced charging sequence of graphene QDs achieved to date²². The measured level separations have been reproduced with the help of tight binding (TB) calculations. Hence, the charging peaks could be assigned to LLs and to particular orbital and valley states. Most notably, we observe quadruplets of charging peaks belonging to a single orbital quantum number of the dot and a partial splitting of single quadruplets into two doublets indicating the lifting of the valley degeneracy (Fig. 1b, d, e). This identification of the multiplet character goes far beyond the results achieved by chemical etching of monolayer graphene QDs²³ or double-sided gating of bilayer graphene QDs²⁴⁻²⁶.

Movable quantum dot

Here, we explore the nanoscale variation of the charging sequence in detail. We use a heterostructure comprised of a SiO₂/graphite support, a hexagonal boron nitride (hBN) substrate, and an active graphene layer on top which are assembled by the dry stacking method^{27,28} (Fig. 1a). The atomic lattices of graphene and hBN are collinearly aligned in order to create a hexagonal superlattice with

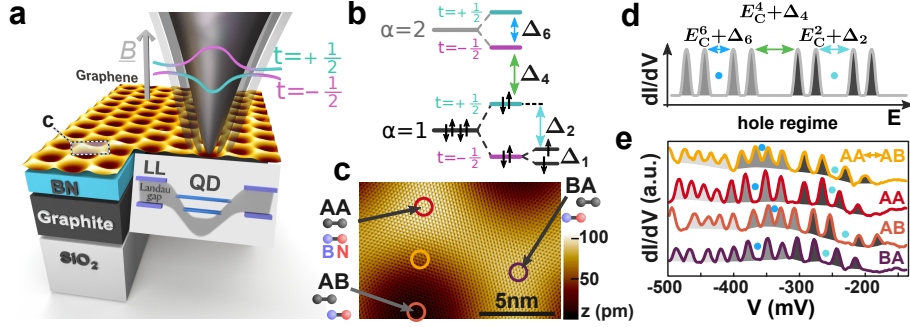


Figure 1: **Edge free quantum dot.** (a) Sketch of the experiment: colored blocks on the left show the stacking sequence $\text{SiO}_2/\text{Graphite}/\text{hBN}/\text{Graphene}$ ²². The STM tip (grey cone) is moved above graphene deposited on BN with its honeycomb lattice collinearly aligned with that of BN (brown-yellow STM image with BN-induced superstructure, $V = 300$ mV, $I = 1$ nA). A perpendicular \underline{B} field (7 T, grey arrow) leads to Landau levels (LL, purple lines) and corresponding Landau gaps (grey area). The electric field of the tip induces band bending (curvature of Landau gap), leading to confined states (blue lines), hence, to a quantum dot (QD). The QD is moved by moving the STM tip above the superstructure (light grey areas around the cone). This modifies the confined state energies as the valley levels $\tau = 1/2$ and $\tau = -1/2$ associated with the K and K' points of the unperturbed band structure (cyan and magenta lines). The rectangle marked **c** indicates the area shown in magnification in **c**. (b) Schematic energy level diagram of the QD. The two orbital levels $\alpha = 1$ and $\alpha = 2$ exhibit valley splitting $E_{\alpha,\tau=+1/2,\sigma} - E_{\alpha,\tau=-1/2,\sigma}$. The Zeeman splitting $E_{\alpha,\tau,\sigma=+1/2} - E_{\alpha,\tau,\sigma=-1/2}$ is small ($\simeq 800$ μeV) and only shown for the lowest valley state. The resulting energy distances Δ_n between adjacent levels are labeled with consecutive n . Δ_n for odd n correspond to Zeeman splittings, which is only displayed for $n = 1$. (c) Atomically resolved STM image of rectangular area marked in **a**, $V = 137$ mV, $I = 0.3$ nA. Different stacking areas (AA, AB, BA) are indicated by arrows with stick and ball models below the labels (C: gray, B: blue, N: red). Colored rings mark the positions of spectra in **e**. (d) Sketch of expected dI/dV peak sequence for hole charging according to the level diagram in **b** using the same colored arrows and the same Δ_n ; E_C^n : charging energy for filling of the n^{th} level. Blue dots highlight valley gaps. (e) dI/dV spectra recorded at the positions encircled by the same color in **c** with corresponding stackings marked (AA \leftrightarrow AB: between AA and AB). Quadruplets of charging peaks, belonging to the same orbital, are shaded equally. Blue dots mark valley transitions. Predominant quadruplet sequences (yellow spectrum), predominant doublet sequences (purple spectrum), or a mixture of both (red and orange spectra) appear, $V_{\text{stab}} = 1$ V, $I_{\text{stab}} = 700$ pA, $V_{\text{mod}} = 4.2$ mV_{rms}, $B = 7$ T, $T = 8$ K.

lattice constant $a = 13.8$ nm originating from the lattice mismatch of graphene and hBN.²⁰ Different stacking regions of the C atoms with respect to the B and N atoms (Fig. 1c) naturally lead to a spatially varying adhesion energy as well as to a spatially varying sublattice symmetry breaking of graphene due to the inequivalent binding sites. The resulting structure has been extensively discussed in the literature^{29–34}. It is known that the most attractive interaction is in the AB areas (Fig. 1c) leading to stretched central regions of graphene with AB stacking and closest contact to the hBN. These areas are surrounded by compressed graphene ridges of different stacking with larger separation to the hBN^{20,30}. However, firm conclusions on the details of the superstructure are difficult to draw, because of the lack of knowledge of details of the van-der-Waals interaction³⁵.

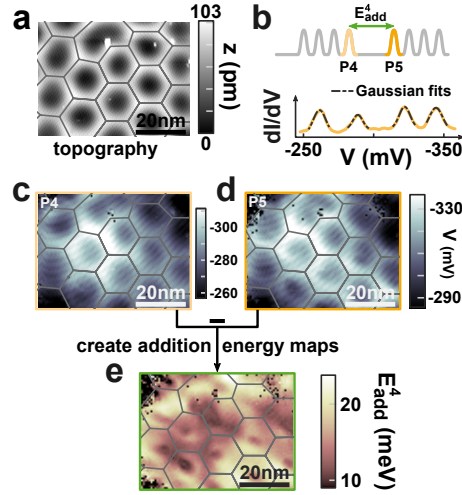


Figure 2: **Addition energy maps from dI/dV spectra.** (a) STM image of graphene collinearly aligned to the h-BN substrate, $V = 400$ mV, $I = 300$ pA, $B = 7$ T, $T = 8$ K. The overlay of grey lines marks the supercell boundary deduced from the topography. (b) Top: sketched charging peak sequence with highlighted peaks P4 and P5 separated by addition energy E_{add}^4 . Bottom: typical dI/dV curve (yellow line) with Gaussian fits (dashed lines) used to determine peak voltages V_{P_n} . (c,d) Maps of V_{P_4} (c) and V_{P_5} (d) of the area of a with identical grey lines overlaid, same parameters for measurement of the map of dI/dV curves as in Fig. 1e. The slight shift of the observed patterns with respect to the grey lines is attributed to a small lateral shift (~ 2 nm) of the tunneling atom with respect to the center of the QD³⁶. (e) E_{add}^4 map deduced by $E_{\text{add}}^4(r) = e \cdot \eta |V_{P_5}(r) - V_{P_4}(r)|$, same grey lines as in a, c, d.

The tip induced graphene QD can be moved across the graphene superstructure by moving the STM tip³⁷. This allows to tune the QD properties, which we probe by tracking the position of the charging peaks within the superlattice.

Therefore, we employ spatially resolved dI/dV spectra (I : tunneling current, V : tip voltage). The resulting maps of charging energies can be directly compared with the corresponding topographic maps recorded simultaneously (Fig. 2a). The charging peaks are fitted by Gaussians (Fig. 2b) for each QD center position \underline{r} , rendering maps of the local variation of the voltage $V_{P_n}(\underline{r})$ of the n^{th} peak, P_n (Fig. 2c, d). Typical variations between the center and the boundary of the hexagonal supercell are $\Delta V_{P_n} \approx 20$ mV. In order to relate this to an energy variation ΔE_n of a particular QD level, we employ a capacitive model yielding $\Delta E_n = e \cdot \eta \cdot \Delta V_{P_n}$ with the lever arm $\eta \simeq 0.5$ ³⁸ and electron charge e . The ΔE_n variations are primarily caused by the spatially varying adhesion energy across the supercell, which indeed varies on the 10 meV-scale according to extensive model calculations³⁰. Figure 2c and d additionally exhibit a long-range variation on the 50 nm scale (amplitude $\Delta V_{P_n} \simeq 40$ mV) which we attribute to the uncontrolled, long-range disorder potential of graphene on hBN with strength of about 20 meV and correlation length of about 50 nm. Similar disorder potentials have been found previously^{39,40}. Note that we carefully avoid lifting of the graphene layer by the tip forces, i.e., we regularly record $I(z)$ curves (z : tip-sample distance) verifying that the current remains below the threshold where a slope change of $\ln(I(z))$ indicates lifting^{41,42}.

Tracking orbital, valley and spin splitting

The group of the first four charging peaks, P1 to P4, is associated with the quadruplet belonging to the first hole orbital of the QD. During the charging of these levels, the QD exhibits a depth of about 100 meV and a width of about 50 nm as known from detailed Poisson calculations^{22,38}. The confined wave functions are labeled $\Psi_{\alpha,\tau,\sigma}$ with orbital quantum number $\alpha = 1$ for the first four peaks, valley quantum number $\tau = \pm\frac{1}{2}$ and spin quantum number $\sigma = \pm\frac{1}{2}$. Analogously, the next four peaks, P5 to P8, belong to the filling of the quadruplet $\Psi_{\alpha=2,\tau,\sigma}$. Subtracting the voltage of the highest peak of the first quadruplet V_{P_4} (Fig. 2c) from that of the lowest peak of the second, V_{P_5} (Fig. 2d), and multiplying by η , yields the locally varying addition energy map $E_{\text{add}}^4(\underline{r}) = e \cdot \eta |V_{P_5}(\underline{r}) - V_{P_4}(\underline{r})|$ (Fig. 2e). It consists of the charging energy $E_C^4(\underline{r})$ and the energy difference $E_{2,-\frac{1}{2},-\frac{1}{2}}(\underline{r}) - E_{1,+\frac{1}{2},+\frac{1}{2}}(\underline{r})$. The latter includes the valley splitting $E_{\alpha,+\frac{1}{2},\sigma}(\underline{r}) - E_{\alpha,-\frac{1}{2},\sigma}(\underline{r})$ and the considerably smaller Zeeman splitting $E_{\alpha,\tau,+\frac{1}{2}}(\underline{r}) - E_{\alpha,\tau,-\frac{1}{2}}(\underline{r}) = g\mu_B B \approx 0.8$ meV ($g = 2$: gyromagnetic factor of graphene, μ_B : Bohr magneton). The dominant contribution comes from the orbital splitting $E_{2,\tau,\sigma}(\underline{r}) - E_{1,\tau,\sigma}(\underline{r})$ as known from tight binding calculations²². Since the wave function size does not change strongly as a function of \underline{r} (see movie in supporting information), the spatial variation of $E_C^4(\underline{r})$ cannot explain the strong spatial variation of $E_{\text{add}}^4(\underline{r})$, which varies by a factor of two. Hence, $E_{\text{add}}^4(\underline{r})$ (Fig. 2e) mostly maps out the orbital-energy spacing between $\alpha = 1$ and $\alpha = 2$, as the quantum dot is moved across the graphene superstructure. Periodic depressions in the center of the supercell reveal the influence of the superstructure on the orbital splitting, while the long-range structure in

Fig. 2e (50 nm scale) is again attributed to the long-range potential disorder.

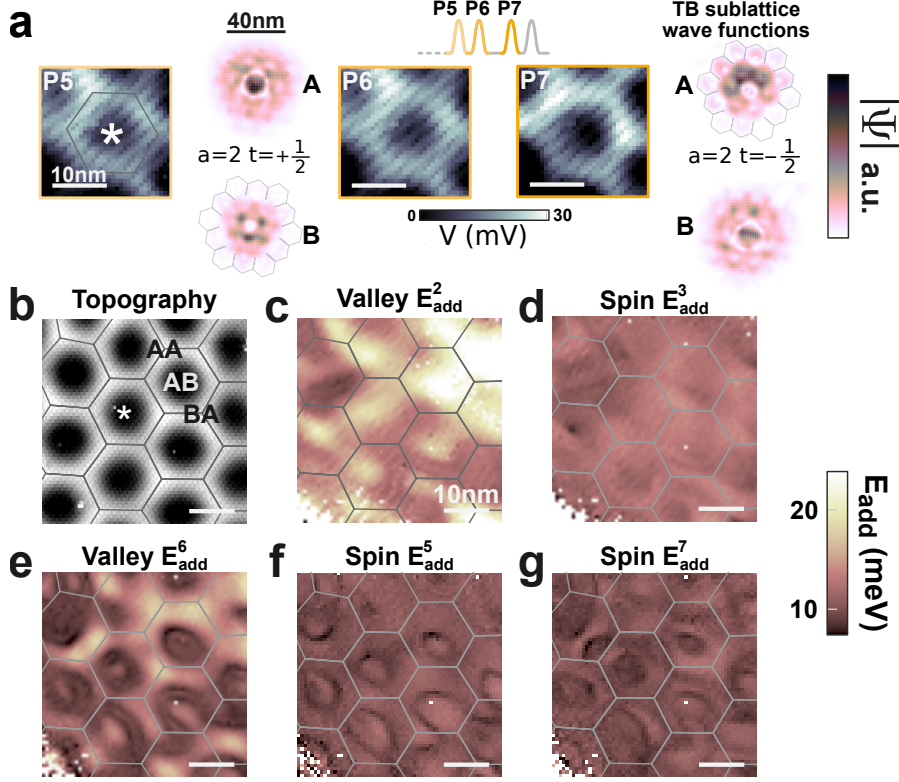


Figure 3: **Addition energy maps for spin and valley gaps.** (a) $V_{P_n}(r)$ displayed at identical contrast for $n = 5, 6, 7$. The corresponding charging sequence is sketched on top. The diagonal stripes are caused by the atomic lattice of graphene via a moiré effect as outlined in supplementary section 6. Asterisk in P5 marks the identical position in **b**. Also shown are the moduli of the wavefunctions for the second hole orbital, $|\Psi_{\alpha=2, \tau=+1/2}|$ and $|\Psi_{\alpha=2, \tau=-1/2}|$, decomposed into the two sublattice contributions, as marked by A and B, as calculated by our TB model. The quantum dot center is in the AB stacking region. Grey honeycombs mark the unit cells of the graphene superstructure. Note the different length scales of $|\Psi|$ maps and V_{P_n} maps. (b) STM image of graphene on hBN including the area of **a**. Grey lines mark supercell boundaries. Different stacking areas (AA, AB, BA) are indicated, $V = 400$ mV, $I = 300$ pA. (c)-(g) $E_{\text{add}}^n(r)$ maps exhibiting identical contrast and belonging to valley and spin gaps as marked, same grey lines as in **b**. Length of all unlabeled scale bars in (a-g): 10 nm. Same parameters for dI/dV spectra as in Fig. 1e.

For clarity, we focus now on the second hole orbital shell $\alpha = 2$ (Fig. 3), while we provide other E_{add}^n maps in the supplementary sections 4 and 5. The

local variation of the voltage peaks belonging to the $\alpha = 2$ quadruplet allows to map out valley and spin splittings in detail. The voltage maps, V_{P6} and V_{P7} , differ on length scales well below that of the supercell size (≈ 10 nm), and much smaller than the size of the QD wave function (diameter ≈ 40 nm, calculated by our TB approach) (Fig. 3a). The addition energy maps (Fig. 3e–g) clearly display short-range supercell-periodic variations on the length scale of 3 nm. These variations appear as dark, ring-like structures around the AB stacking region of the supercell in the valley addition energy map E_{add}^6 . Similar, but slightly narrower rings appear in the spin addition energy maps E_{add}^5 and E_{add}^7 .

Analyzing the valley splitting maps

We analyze these remarkably strong nanometer scale variations by performing TB calculations^{31,43}. The calculations feature three major ingredients: (i) the sublattice-independent local on-site potential $V_0(\underline{r})$ representing the spatially varying adhesion energy, (ii) the sublattice symmetry-breaking on-site potential $V_z(\underline{r})$ caused by the spatially varying stacking, and (iii) a locally varying hopping amplitude $\gamma(\underline{r})$ accounting for strain which also breaks sublattice symmetry^{18,34,42}. We use an average distance between graphene and hBN of 3.3 Å, originating from DFT calculations employing the random phase approximation²⁹ and consistent with cross sectional electron microscopy data⁴⁴. To obtain locally varying tight-binding parameters, we first employ a continuum model of graphene with known elastic constants³² subject to the potential landscape from the hBN³⁰. This reproduces the corrugation of 70 pm and the strain variation of 2 %, as visible in the STM data (Fig. 2a)²⁰. Based on the resulting membrane shape of the graphene layer, a molecular dynamics simulation using isotropic Lenard-Jones potentials is employed to obtain the atomically resolved strain, the variations in the local distance between hBN and graphene, and the local stacking configuration³⁸. Using these input parameters, we determine $V_0(\underline{r})$, $V_z(\underline{r})$ and $\gamma(\underline{r})$ from our own DFT calculations³⁸. The potentials and hopping parameters provide, in turn, the input to our third-nearest neighbor TB calculation of the QD states^{22,31,43}. We emphasize that no freely adjustable parameter enters our simulation. More details are described in supplementary sections 7-10.

In agreement with the experiment, the calculated energies of the two valley states of the second orbital feature a pronounced variation with QD position (Fig. 4a–d). To disentangle the influence of strain and of the hBN substrate interaction, we analyze the contributions due to $V_0(\underline{r})$, $V_z(\underline{r})$, and $\gamma(\underline{r})$ separately. While V_0 (Fig. 4a) introduces local variations of the energy of the hole orbital $\alpha = 2$ along the path AA \leftrightarrow AB \leftrightarrow BA, it does not lift the fourfold valley and spin degeneracy. $V_z(\underline{r})$, by contrast, lifts the degeneracy between the two valley states $\Psi_{2,+\frac{1}{2},\sigma}$ and $\Psi_{2,-\frac{1}{2},\sigma}$ and even leads to an inversion of the energetic order in the AA region of the superlattice, i.e., a change of sign of $E_{2,+\frac{1}{2},\sigma} - E_{2,-\frac{1}{2},\sigma}$ (Fig. 4b). However, only when the contribution of strain is accounted for through $\gamma(\underline{r})$, which inverts the sign of the valley splitting in the

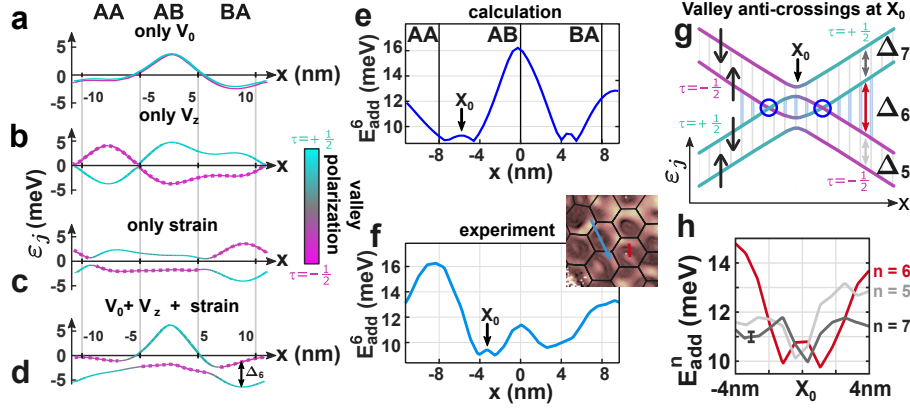


Figure 4: **Valley crossing.** (a)–(d) TB energies (ϵ_j) of the two valley states of the second QD hole orbital ($\alpha = 2$) as a function of the center position of the QD. Different stackings at this center along a high symmetry line of the superstructure are given on top. The valley polarization is color coded. Panel (a) considers only the sublattice independent potential $V_0(r)$, (b) only the sublattice symmetry breaking on-site potential $V_z(r)$, (c) only the varying hopping parameter $\gamma(r)$ due to strain, and (d) the sum of all three contributions. The valley splitting Δ_6 determining the spatial variation in e is indicated by a double arrow in d, $B = 7$ T. (e) Theoretical prediction for E_{add}^6 based on d (supplementary section 8). (f) Experimental addition energy E_{add}^6 along the arrow of the same color as in the inset (same $E_{\text{add}}^6(r)$ map as Fig. 3d). The x -axis is aligned to the stackings marked in e. X_0 indicates a feature attributed to the influence of spin splitting at the valley crossing. The origin in (a)–(f) is chosen in the center of the AB region. (g) Schematic evolution of the state energies for a crossing of two valley states ($\tau = +1/2$: cyan, $\tau = -1/2$: magenta). A spatially constant spin splitting (levels marked by black spin arrows) is added. The resulting energy differences Δ_n are marked by double arrows. An anticrossing emerges at X_0 as deduced from d. Blue circles mark spin level crossings. (h) Experimental $E_{\text{add}}^n(r)$ along the red line in the inset of f, belonging to one preferential valley gap (red) and two spin gaps (grey). A typical error bar, resulting from the Gaussian fits of the dI/dV peaks, is shown.

BA region (Fig. 4c), the correct overall level ordering with level inversion in the AB region, as seen in our experiment, emerges (Fig. 4d).

The addition energies in both, the TB model (Fig. 4e) and the experiment (Fig. 4f), show the same variation of about 6 meV and the same order of maxima and minima along the displacement coordinate x . Hence, we attribute the periodically appearing rings encircling the AB region (Fig. 3e), which correspond to the bump at X_0 with adjacent minima in Fig. 4e, as the positions of an inversion of valley ordering. Remaining quantitative differences between TB model and experiment (Fig. 4e, f) are attributed to disorder, most likely due to

residual irregular strains caused by the non-perfect collinear alignment between graphene and hBN. The resulting disorder is directly visible as irregularities in the unit cell of the superstructure (Fig. 2a, Fig. 3b) and also explains the irregular distortions of the rings around the AB region.

The assignment of the rings around the AB region to valley inversions is corroborated by the appearance of the small bump in the ring minimum, marked X_0 in Fig. 4e–h. It is found in theory and experiment with a height of less than 1 meV. The theoretical level diagram (Fig. 4g) provides a simple explanation: the bump is the result of the additional spin splitting during the passage through the crossing of valley levels. At X_0 , E_{add}^6 consists of E_C^6 and the spin splitting $\left| E_{2,\tau,\frac{1}{2}} - E_{2,\tau,-\frac{1}{2}} \right| \approx 800 \mu\text{eV}$ reduced by anti-crossing contributions. In contrast, the two spatially offset crossings of valley states with different spins (blue circles in Fig. 4g) feature only E_C^6 , resulting in the minima around the bump. Figure 4g also explains the rings in the spin splitting maps (Fig. 3f, g), which are simply the reduced Δ_5 and Δ_7 at X_0 . The spatial alignment of the bump in Δ_6 and the minima in $\Delta_{5,7}$ are nicely corroborated by the experiment (Fig. 4h).

While we have focused here on the valley splitting of the second hole state, similar ring-like structures encircling the AB area are also found for the third hole orbital $\alpha = 3$ with tunability of the valley crossing up to 15 meV (Fig. S2)³⁸. In contrast, the first hole orbital $\alpha = 1$ (Fig. 3c, e) exhibits a valley tunability of about 7 meV without inversion of the valley ordering. On the electron side, the additional charging of defects within the h-BN⁴⁵ complicates the analysis⁴⁶, but some ring-like structures indicating valley inversion can also be spotted³⁸. Data recorded with another microtip at two different B fields exhibit very similar features (Fig. S3). Moreover, the energy range of valley tunability remains independent of B , corroborating that the valley tuning is caused by the interaction with the substrate and not by the B field. For example, the strength of the exchange enhancement would vary with B ³⁸. In addition, it turns out to be one order of magnitude too weak to explain the experimentally observed valley tuning (supplementary section 12).

A simple estimate clarifies the resulting strength of the valley splitting of about 10 meV. The sublattice breaking interactions itself ($V_z(r)$, $\gamma(r)$) spatially vary by about 100 meV as deduced from our DFT calculations³⁸. Hence, shifting about 10% of the hole density of a state ($\propto |\Psi|^2$) from the unfavorable AB to the favorable AA region is sufficient to account for variations of the valley splitting of about 10 meV. Indeed, our detailed TB calculations find that the $\alpha = 2$ wave function covers about ten unit cells (Fig. 3a) and adjusts mainly its distribution within the central unit cell due to the changing potential landscape (supplemental movie).

Conclusions and outlook

The revealed tunability of a valley splitting by up to 15 meV surpasses the highest reported values of valley tuning for other potentially nuclear spin free host

materials (Si/SiO₂, 500 μ eV)⁵ by more than one order of magnitude. Hence, it might be exploited at temperatures up to 4 K. Most intriguingly, the crossings of valley and spin levels as depicted in Fig. 4g can be used to initialize superposition states of spin and valley degrees of freedom^{2,47}. This could be the starting point to determine the coherence⁴⁸ of both types of states in graphene for the first time. The required interaction of the levels rendering the depicted crossings into anti-crossings is naturally provided by the spatially varying sublattice potential coupling opposite valley states (Fig. 4d). We note in passing that the breaking of the valley degeneracy is also the central requirement for exchange-based spin qubits, which could provide an all electrical spin qubit operation in graphene⁴⁹. A possible device setup for these purposes could employ side gates for moving gate-based QDs and, hence, for providing the valley tuning. Edge states, belonging to each LL, can provide tunable source and drain contacts (supplementary section 13).

Finally, we emphasize that the approach of designed van-der-Waals heterostructures^{19–21} for a versatile tuning of electronic degrees of freedom might be extended to physical spin schemes by using an atomically varying spin orbit interaction as present, e.g., for graphene on WSe₂⁵⁰.

Acknowledgements

The authors appreciate helpful discussions with C. Stampfer, H. Bluhm, R. Bindel, M. Liebmann, and K. Flöhr as well as the assisting during the measurements by A. Georgi. NMF, PNI and MM acknowledge support from the European Union Seventh Framework Programme under Grant Agreement No. 696656 (Graphene Flagship) and the German Science foundation (Li 1050-2/2 through SPP-1459), LAC, JB and FL from the Austrian Fonds zur Förderung der wissenschaftlichen Forschung (FWF) through the SFB 041-ViCom and doctoral college Solids4Fun (W1243). TB calculations were performed on the Vienna Scientific Cluster. RVG, AKG and KSN also acknowledge support from EPSRC (Towards Engineering Grand Challenges and Fellowship programs), the Royal Society, US Army Research Office, US Navy Research Office, US Airforce Research Office. KSN is also grateful to ERC for support via Synergy grant Hetero2D. AKG was supported by Lloyds Register Foundation. PNI acknowledges the support from the Hungarian Academy of Sciences Lendület grant no. LP2017-9/2017.

Author contributions

N.M.F. carried out the STM measurements with assistance of P.N.I. and C.H. and evaluated the experimental data under supervision of P.N.I. and M.M.; P.N.I. has performed the strain calculations, while T.R., F.L., and L.A.C. have contributed DFT and TB calculations; C.R.W., Y.C., R.V.G., A.K.G. and K.S.N. provided the sample; M.M. conceived and coordinated the project partly together with N.M.F., P.N.I. and F.L.; the comparison between theory and experiment has been conducted by N.M.F., M.M., F.L., and P.N.I.; M.M., N.M.F.,

P.N.I. and F.L. wrote the manuscript with contributions from all authors.

References

- [1] Ladd, T. D. *et al.* Quantum computers. *Nature* **464**, 45–53 (2010).
- [2] Pioro-Ladriere, M. *et al.* Electrically driven single-electron spin resonance in a slanting zeeman field. *Nat. Phys.* **4**, 776–779 (2008).
- [3] Wu, X. *et al.* Two-axis control of a singlet-triplet qubit with an integrated micromagnet. *Proc. Natl. Acad. Sci. U.S.A.* **111**, 11938–11942 (2014).
- [4] Abanin, D. A. *et al.* Giant Nonlocality Near the Dirac Point in Graphene. *Science* **332**, 328–330 (2011).
- [5] Yang, C. H. *et al.* Spin-valley lifetimes in a silicon quantum dot with tunable valley splitting. *Nat. Commun.* **4**, 2069 (2013).
- [6] Shimazaki, Y. *et al.* Generation and detection of pure valley current by electrically induced Berry curvature in bilayer graphene. *Nat. Phys.* **11**, 1032–1036 (2015).
- [7] Sui, M. *et al.* Gate-tunable topological valley transport in bilayer graphene. *Nat. Phys.* **11**, 1027–1031 (2015).
- [8] Ju, L. *et al.* Topological valley transport at bilayer graphene domain walls. *Nature* **520**, 650–655 (2015).
- [9] Wallbank, J. R. *et al.* Tuning the valley and chiral quantum state of Dirac electrons in van der Waals heterostructures. *Science* **353**, 575–579 (2016).
- [10] Rahman, R. *et al.* Engineered valley-orbit splittings in quantum-confined nanostructures in silicon. *Phys. Rev. B* **83**, 195323 (2011).
- [11] Gokmen, T. *et al.* Parallel magnetic-field tuning of valley splitting in alas two-dimensional electrons. *Phys. Rev. B* **78**, 233306 (2008).
- [12] Kobayashi, T. *et al.* Resonant tunneling spectroscopy of valley eigenstates on a donor-quantum dot coupled system. *Appl. Phys. Lett.* **108**, 152102 (2016).
- [13] Gamble, J. K. *et al.* Valley splitting of single-electron si MOS quantum dots. *Appl. Phys. Lett.* **109**, 253101 (2016).
- [14] Scarlino, P. *et al.* Dressed photon-orbital states in a quantum dot: Intervalley spin resonance. *Phys. Rev. B* **95**, 165429 (2017).
- [15] Mi, X., Péterfalvi, C. G., Burkard, G. & Petta, J. High-resolution valley spectroscopy of Si quantum dots. *Phys. Rev. Lett.* **119**, 176803 (2017).

- [16] Xiao, D., Yao, W. & Niu, Q. Valley-contrasting physics in graphene: Magnetic moment and topological transport. *Phys. Rev. Lett.* **99**, 236809 (2007).
- [17] Pesin, D. & MacDonald, A. H. Spintronics and pseudospintronics in graphene and topological insulators. *Nat. Mater.* **11**, 409–416 (2012).
- [18] Castro Neto, A. H., Guinea, F., Peres, N. M. R., Novoselov, K. S. & Geim, A. K. The electronic properties of graphene. *Rev. Mod. Phys.* **81**, 109–162 (2009).
- [19] Geim, A. K. & Grigorieva, I. V. Van der waals heterostructures. *Nature* **499**, 419–425 (2013).
- [20] Woods, C. R. *et al.* Commensurate-incommensurate transition in graphene on hexagonal boron nitride. *Nat. Phys.* **10**, 451–456 (2014).
- [21] Novoselov, K. S., Mishchenko, A., Carvalho, A. & Castro Neto, A. H. 2D materials and van der Waals heterostructures. *Science* **353**, 461–470 (2016).
- [22] Freitag, N. M. *et al.* Electrostatically confined monolayer graphene quantum dots with orbital and valley splittings. *Nano Lett.* **16**, 5798–5805 (2016).
- [23] Bischoff, D. *et al.* Localized charge carriers in graphene nanodevices. *Appl. Phys. Rev.* **2**, 031301 (2015).
- [24] Allen, M. T., Martin, J. & Yacoby, A. Gate-defined quantum confinement in suspended bilayer graphene. *Nat. Commun.* **3**, 934 (2012).
- [25] Goossens, A. M. *et al.* Gate-defined confinement in bilayer graphene-hexagonal boron nitride hybrid devices. *Nano Lett.* **12**, 4656–4660 (2012).
- [26] Müller, A. *et al.* Bilayer graphene quantum dot defined by topgates. *J. Appl. Phys.* **115**, 233710 (2014).
- [27] Mayorov, A. S. *et al.* Micrometer-scale ballistic transport in encapsulated graphene at room temperature. *Nano Lett.* **11**, 2396–2399 (2011).
- [28] Kretinin, A. V. *et al.* Electronic properties of graphene encapsulated with different two-dimensional atomic crystals. *Nano Lett.* **14**, 3270–3276 (2014).
- [29] Sachs, B., Wehling, T. O., Katsnelson, M. I. & Lichtenstein, A. I. Adhesion and electronic structure of graphene on hexagonal boron nitride substrates. *Phys. Rev. B* **84**, 195414 (2011).
- [30] van Wijk, M. M., Schuring, A., Katsnelson, M. I. & Fasolino, A. Moiré patterns as a probe of interplanar interactions for graphene on h-bn. *Phys. Rev. Lett.* **113**, 135504 (2014).

- [31] Chizhova, L. A., Libisch, F. & Burgdörfer, J. Graphene quantum dot on boron nitride: Dirac cone replica and hofstadter butterfly. *Phys. Rev. B* **90**, 165404 (2014).
- [32] San-Jose, P., Gutiérrez-Rubio, A., Sturla, M. & Guinea, F. Spontaneous strains and gap in graphene on boron nitride. *Phys. Rev. B* **90**, 075428 (2014).
- [33] Slotman, G. J. *et al.* Effect of structural relaxation on the electronic structure of graphene on hexagonal boron nitride. *Phys. Rev. Lett.* **115**, 186801 (2015).
- [34] Jung, J. *et al.* Moiré band model and band gaps of graphene on hexagonal boron nitride. *Phys. Rev. B* **96**, 085442 (2017).
- [35] Ambrosetti, A., Ferri, N., DiStasio, R. A., Jr. & Tkatchenko, A. Wavelike charge density fluctuations and van der Waals interactions at the nanoscale. *Science* **351**, 1171–1176 (2016).
- [36] Morgenstern, M. *et al.* Origin of landau oscillations observed in scanning tunneling spectroscopy on n-inas(110). *Phys. Rev. B* **62**, 7257–7263 (2000).
- [37] Dombrowski, R., Steinebach, C., Wittneven, C., Morgenstern, M. & Wiesendanger, R. Tip-induced band bending by scanning tunneling spectroscopy of the states of the tip-induced quantum dot on inas(110). *Phys. Rev. B* **59**, 8043–8048 (1999).
- [38] Freitag, N. *et al.* *see supplementary information* .
- [39] Xue, J. M. *et al.* Scanning tunnelling microscopy and spectroscopy of ultra-flat graphene on hexagonal boron nitride. *Nat. Mater.* **10**, 282–285 (2011).
- [40] Decker, R. *et al.* Local electronic properties of graphene on a bn substrate via scanning tunneling microscopy. *Nano Lett.* **11**, 2291–2295 (2011).
- [41] Mashoff, T. *et al.* Bistability and Oscillatory Motion of Natural Nanomembranes Appearing within Monolayer Graphene on Silicon Dioxide. *Nano Lett.* **10**, 461–465 (2010).
- [42] Georgi, A. *et al.* Tuning the Pseudospin Polarization of Graphene by a Pseudomagnetic Field. *Nano Lett.* **17**, 2240–2245 (2017).
- [43] Libisch, F., Rotter, S., Güttinger, J., Stampfer, C. & Burgdörfer, J. Transition to landau levels in graphene quantum dots. *Phys. Rev. B* **81**, 245411 (2010).
- [44] Haigh, S. J. *et al.* Cross-sectional imaging of individual layers and buried interfaces of graphene-based heterostructures and superlattices. *Nat. Mater.* **11**, 764–767 (2012).

- [45] Wong, D. *et al.* Characterization and manipulation of individual defects in insulating hexagonal boron nitride using scanning tunnelling microscopy. *Nat. Nanotechnol.* **10**, 949–953 (2015).
- [46] Morgenstern, M., Freitag, N., Nent, A., Nemes-Incze, P. & Liebmann, M. Graphene quantum dots probed by scanning tunneling microscopy. *Ann. d. Phys.* **529**, 1700018 (2017).
- [47] Petta, J. *et al.* Coherent manipulation of coupled electron spins in semiconductor quantum dots. *Science* **309**, 2180–2184 (2005).
- [48] Elzerman, J. M. *et al.* Single-shot read-out of an individual electron spin in a quantum dot. *Nature* **430**, 431 (2004).
- [49] Trauzettel, B., Bulaev, D. V., Loss, D. & Burkard, G. Spin qubits in graphene quantum dots. *Nat. Phys.* **3**, 192–196 (2007).
- [50] Wang, Z. *et al.* Origin and Magnitude of ‘Designer’ Spin-Orbit Interaction in Graphene on Semiconducting Transition Metal Dichalcogenides. *Phys. Rev. X* **6**, 041020 (2016).

Methods

The sample was prepared by exfoliating graphite flakes on a SiO₂ substrate, followed by two consecutive dry transfers^{27,28} of 30 nm thick hexagonal hBN and monolayer graphene, respectively. During the graphene transfer, we took care to minimize the angular misalignment between the graphene lattice and the hBN lattice. Remaining small misalignments in the 0.1° regime cannot be excluded²⁰. Moreover, a few small bubbles between the graphene and the h-BN appear after transfer (see chapter S7 of Ref.⁴²). Both of these effects lead to mechanical stresses which perturb the graphene/BN superlattice in period or shape⁵¹ (Fig. 2a and 3b of the main text). The graphene flake overlaps the hBN completely. This avoids insulating areas, which would be hazardous to the STM tip, but does not allow for back-gate operation. Finally, electrical Cr/Au contacts (2 nm/100 nm) are evaporated onto the large bottom graphite flake via a shadow mask. Optical images of the device structure are available in the supplement of a previous publication²².

STM and STS measurements are performed in a home-built ultra-high-vacuum STM chamber operating at temperature $T = 8$ K and in magnetic fields up to $B = 7$ T perpendicular to the surface.⁵² Tungsten tips are prepared by etching of W wires, which are subsequently controlled with an optical microscope. The microtips are transferred into the STM within the UHV chamber, where they are reshaped by controlled indentation into the Au(111) surface of a Au bead.⁵³ Thereby, they form a Au apex of a few 10 nm in length as cross-checked by electron microscopy. We characterize the tips in-situ by mapping the topographic and spectroscopic features of the Au(111) surface prior to exchanging the Au crystal by the graphene sample. Scanning tunneling microscopy

(STM) images are recorded in constant current mode at tunneling current I and tip voltage V . Differential conductance curves $dI/dV(V)$ are recorded by lock-in detection using a modulation voltage with amplitude $V_{\text{mod}} = 2-5 \text{ mV}_{\text{rms}}$ and frequency $f_{\text{mod}} = 1223 \text{ Hz}$. After stabilizing the tip-sample distance at stabilization voltage V_{stab} and stabilization current I_{stab} , the feedback loop is opened for the $dI/dV(V)$ recording. During the recording, the tip-sample distance is changed at a rate of 50 pm/V , approaching the sample by 0.5 \AA while sweeping V from 1 V to 0 V and retracting it by the same distance while continuing to -1 V . This compensates for the changing height of the tunneling barrier as a function of V .⁵⁴ The resulting change in tip-sample capacitance is below 2.5% .²² It is, thus, neglected, since much smaller than other capacitance uncertainties (see below). Additionally, we normalize the dI/dV data according to $(dI/dV(V))/I(V_{\text{stab}})$ with $I(V_{\text{stab}})$ being the firstly detected current after opening the feedback loop. This compensates for the influence of vibrations during the stabilization process.

We focus on the first two orbital states for confined holes, originating from LL_{-1} (see below), as they capture the essential features. On the electron side, charging of randomly distributed defects in the hBN⁴⁵ impedes an unambiguous analysis of the QD charging patterns (see Fig. S2 of the supplement)²².

Data availability

The data that support the plots within this paper and other findings of this study are available from the corresponding author upon reasonable request.

Additional information

Supplementary information is available in the online version of the paper. Reprints and permission information is available online at www.nature.com/reprints. Correspondence and requests for materials should be addressed to M.M.

References

- [51] Jiang, Y. *et al.* Visualizing strain-induced pseudomagnetic fields in graphene through an hBN magnifying glass. *Nano Lett.* **17**, 2839–2843 (2017).
- [52] Mashoff, T., Pratzner, M. & Morgenstern, M. A low-temperature high resolution scanning tunneling microscope with a three-dimensional magnetic vector field operating in ultrahigh vacuum. *Rev. Sci. Instr.* **80**, 053702 (2009).
- [53] Voigtländer, B., Cherepanov, V., Elsaesser, C. & Linke, U. Metal bead crystals for easy heating by direct current. *Rev. Sci. Instr.* **79**, 033911 (2008).

- [54] Feenstra, R. Tunneling spectroscopy of the (110)-surface of direct-gap III-V semiconductors. *Phys. Rev. B* **50**, 4561–4570 (1994).